



Helium irradiation-induced ultrahigh hardening in niobium

Jing-Ting Li^a, Irene J. Beyerlein^{b,c,1}, Wei-Zhong Han^{a,*}

^a Center for Advancing Materials Performance from the Nanoscale, State Key Laboratory for Mechanical Behavior of Materials, Xi'an Jiaotong University, Xi'an 710049, PR China

^b Department of Mechanical Engineering, University of California, Santa Barbara, CA 93106-5070, USA

^c Materials Department, University of California, Santa Barbara, CA 93106-5070, USA

ARTICLE INFO

Article history:

Received 28 July 2021

Revised 3 November 2021

Accepted 11 January 2022

Available online 14 January 2022

Keywords:

Niobium
Irradiation
Helium
Hardening
Complex

ABSTRACT

In this work, using *in-situ* uniaxial tensile and compressive testing, microscopy, and theoretical analysis, we study the mechanism underlying the ultrahigh irradiation hardening in niobium (Nb). We show that irradiated Nb pillar exhibits a more than two-fold increase in the yield stress. With *in-situ* mechanical testing, we observe that He bubbles in Nb promote dislocation nucleation and multiple slip systems. The Nb pillars with 1.2 nm He bubbles fail by bubble coalescence and form a faceted fracture surface. In contrast, the Nb pillars with 8 nm He bubbles fail by bubble elongation and fragmentation. A theoretical analysis of the hardening contribution based solely on the density and size of He bubbles finds that it is less than one third of the experimentally observed hardening. To explain the large gap between the model and the experiment, we propose that the ultrahigh irradiation hardening originates from a large quantity of atomic-size, undetectable He-vacancy (He-V) complexes. The implanted He ions only account for less than 50% percent in the visible He bubbles, while most of them bind to vacancies to form stable He-V complexes that are distributed throughout the lattice. The strong interaction between dislocations and high density of He-V complexes is the chief source for the remarkable irradiation hardening observed in Nb.

© 2022 Acta Materialia Inc. Published by Elsevier Ltd. All rights reserved.

1. Introduction

Refractory body-centered-cubic (BCC) metals, such as niobium (Nb), are candidate materials for nuclear applications and heating elements due to their high melting point, excellent high-temperature strength, and radiation tolerance [1,2]. Continuous ion bombardment produces many vacancies and interstitials in nuclear reactor components. These point defects tend to cluster and evolve into larger defect variants, such as dislocation loops [3–5], voids [4,6], stacking fault tetrahedra [7,8], and gas bubbles [9,10]. Radiation defects can pose a significant threat to the operation of structural materials in a nuclear reactor. At low temperatures ($0.3-0.4T_M$, T_M is the melting temperature) and relatively low doses (0.001 to 0.1 dpa), radiation hardening can be accompanied by reductions in uniform elongation and fracture toughness [11–14]. At intermediate temperatures ($0.3-0.6 T_M$), accumulation of vacancies causes swelling, which produces volumetric expansion of the component and stress concentrations [15]. At high temperatures

(> $0.5 T_M$), the exceptionally large cavities tend to accumulate along grain boundaries and induce premature intergranular failure [16]. To mitigate radiation damage, the mechanisms of radiation defect production, migration, clustering, and their interaction with dislocations need to be well understood.

The hardening mechanism provided by irradiation-induced helium (He) bubbles has received particular attention [17–20]. In small-volume face-centered cubic (FCC) Cu, nanoscale He bubbles enhance yield strength and improve deformation stability but lead to a short uniform deformation stage during tensile testing [17]. Under straining, nanoscale He bubbles play a combined role of acting as shearable obstacles and active internal dislocation sources and is the origin of improved plasticity and toughness in irradiated Cu [17,18]. In hexagonal close-packed (HCP) Zr, irradiation hardening is often associated with the production of <a> or <c>-type dislocation loops, which are obstacles to dislocation glide on prismatic planes [19]. Yet, He bubbles in irradiated Zr, less than 8 nm in size, can also increase the critical resolved shear stress (CRSS) for prismatic slip. The effect does, however, depend on bubble size. Once the bubbles are larger than 8 nm, bubble-softening ensues, due to deformation-induced bubble coalescence [17–20].

The mechanical properties of irradiated BCC metals have also been explored, but the hardening mechanism has yet to be fully understood [21–24]. The neutron irradiated Nb showed a 1.4 to

* Corresponding author.

E-mail address: wzhanxjtu@mail.xjtu.edu.cn (W.-Z. Han).

¹ Irene J. Beyerlein was an Editor of the journal during the review period of the article. To avoid a conflict of interest, Irene J. Beyerlein was blinded to the record and another editor processed this manuscript.

2 times greater hardening than that predicted from calculations based on observable irradiation defects [22]. These discrepancies have been attributed to the interdependence between interstitial impurities and radiation defects, but the main hardening mechanism still remains unclear [22]. In He irradiated tungsten, He solutes were found to contribute substantially to irradiation hardening, while the other radiation defects, such as dislocation loops, He bubbles and vacancy-type defects, provided almost similar, relatively smaller contributions [25]. Likewise, in neutron irradiated reduced-activation ferritic/martensitic steels, dislocation-loop hardening by the Orowan mechanism was found insufficient in explaining the measured irradiation-hardening in experiment, and the backstress arising from pile ups of dislocations in channels was proposed as the extra contributor to irradiation hardening [26]. In addition, for irradiated Fe, when the He-to-vacancy ratio is low, ranging from 0 to 1, the hardening contribution from He bubbles is constant. However, with higher He-to-vacancy (He-V) ratios, the contribution from He bubbles gradually decreases [27]. Therefore, at present, the hardening mechanism in irradiated BCC metals is still under debate [22–30], calling for an irradiation defects-based reasonable explanation. Recently, the ultrahigh irradiation hardening in He irradiated tungsten was attributed to a large fraction of very stable atomic-sized hidden He-V complexes [31]. The applicability of this point-defect complex mechanism to other BCC metals, however, needs to be confirmed.

In this study, we investigate the mechanical properties of He irradiated Nb pillars with different levels of He concentration. After irradiation, we observed exceptional hardening, more than a two-fold increase in the yield strength, and a steep strain hardening rate. By counting the total number of implanted He and the number of He atoms in the transmission electron microscope (TEM)-visible bubbles, we find that more than 50% of the undetected He atoms likely lie within the Nb lattice. We propose that the remaining He have combined with small vacancy clusters to form stable He-vacancy (He-V) complexes and serve as the chief hardening component in irradiated Nb.

2. Materials and methods

2.1. Sample preparation

Single crystal Nb is used as a model material in this study. Nb thin foils with a thickness of 30 μm were irradiated with 400 keV He ions at 400 °C using a NEC 400 kV Implanter. The ion beam was rastered and the sample was scanned line by line. Two different fluences of He implantation were designed to fabricate samples with different levels of He: 2.0×10^{17} ion/cm² and 5.0×10^{17} ion/cm². The resulting samples are denoted as Nb-S (with 14 at.% of He, small bubbles) and Nb-M (with 29 at.% of He, medium-sized bubbles). One of the Nb thin foils was implanted to the same fluence of 5.0×10^{17} ion/cm² but then further annealed in a tube furnace at 1000 °C for 1 h under a vacuum of $\sim 5 \times 10^{-5}$ Pa to increase the bubble size. This sample is referred to as Nb-L (with 29 at.% of He, but large bubbles). For comparison, another single crystal Nb with 30 μm thickness was irradiated with 800 keV krypton at a temperature of 400 °C to a fluence of 5.0×10^{15} ion/cm² and named the Kr-Nb sample. The peak damage in this Kr-irradiated sample is 36 dpa.

2.2. In-situ nanomechanical test

A series of micro-tensile and micro-compressive samples, with diameter D ($D \equiv \sqrt{A}$, where A is the cross-sectional area) ranging from 100 to 300 nm, were cut, using focus ion beam (FIB) with beam current in the range of 21 nA to 9.3 pA at accelerate voltage of 30 kV, at a depth of 820 nm in the He implanted samples, and

at a depth of 210 nm in the Kr ion irradiated samples. All these samples have similar sample dimension in order to remove sample size effect on the mechanical behavior. The radiation damage in the Kr-Nb fabricated at the depth of 210 nm is 23.4 dpa and the Kr concentration is 0.4 at.%. The damage level of the Kr-Nb sample at the depth of 210 nm is like that of the Nb-L sample at a depth of 820 nm. To perform high-resolution *in-situ* mechanical loading, push-to-pull (PTP) samples were also fabricated by FIB [32]. Quantitative *in-situ* mechanical tests were conducted using a Hysitron PicoIndenter (PI95) inside a TEM under the displacement-control mode. The displacement rate was programmed to be 5 nm/s in compression and 1.5 nm/s in tension, which corresponds to an initial strain rate of $\sim 5 \times 10^{-3}$ s⁻¹. Fig. 1 illustrates the experimental process, including the orientations of the sample for implantation and *in-situ* mechanical testing. The irradiation damage and He concentration as a function of depth were obtained using Stopping and Range of Ions in Solids (SRIM) in the full cascade mode and using an average threshold displacement energy of 35 eV for Nb [33]. The depth-dependent concentration of implanted He ion consistent well with the SRIM prediction [17,34].

3. Results

3.1. He bubbles in the implanted Nb

Fig. 2(a)–(c) show TEM images of typical He bubbles in the Nb-S, Nb-M and Nb-L samples. These TEM foils were taken from the peak He concentration region, at depths ranging from 720 to 920 nm, in the irradiated Nb single crystals. The He bubbles are spherical in the Nb-S and Nb-M samples, and appear to be partly faceted in the Nb-L sample. As we designed, the bubbles varied in size in these three samples. The average bubble diameter is $D_b = 1.2$ nm for Nb-S, $D_b = 1.9$ nm for Nb-M and $D_b = 8.1$ nm for Nb-L. He irradiation-induced self-interstitial atoms mainly diffuse to the sample surface or to the deeper region of the sample [34].

Fig. 2(d) shows the surface morphology and cross-section view of the Nb-L sample. After annealing, spherical surface blisters, or bumps, occupying near 50% of the surface, have formed. To examine the microstructures underneath, we cut through one of the bumps using FIB. A thin layer of Nb of thickness ~ 800 nm, has delaminated from the sample, forming an arciform shape. The thickness of this spalled layer just equals the distance from the sample surface to the peak He concentration, indicating that the blistering is induced by the coalescence of He bubbles in this region under high temperature annealing. Because of the strong binding between He and vacancies (-1.75 eV), even we annealed the sample at 1000 °C for 1 h, the He bubble size increase obviously, but the peak He concentration still located in the depth of ~ 800 nm. Therefore, the implanted He ions cannot diffuse far even annealed at high temperature.

3.2. In-situ compression and tension of the Nb-S pillars

Fig. 3(a) and (b) shows typical compressive and tensile responses of the pure Nb and Nb-S pillars with $D = 110$ nm. The loading direction is along [101]. Under compression, the pure Nb pillar has a yield stress of 1.44 GPa. The plastic flow of this sample shows a series of strain bursts. The Nb-S sample, however, has a much higher yield stress of 2.85 GPa and followed by a significant strain hardening rate of 13 GPa. Moreover, the plastic flow in Nb-S is relatively stable, containing no strain bursts. This behavior is like the compressive properties of other metals containing He bubbles [17–21]. Fig. 3(c)–(e) show the morphology of pillars before and after compression. After deformation, localized shear bands form in pure Nb pillar and produce sharp slip steps on the pillar surface, as

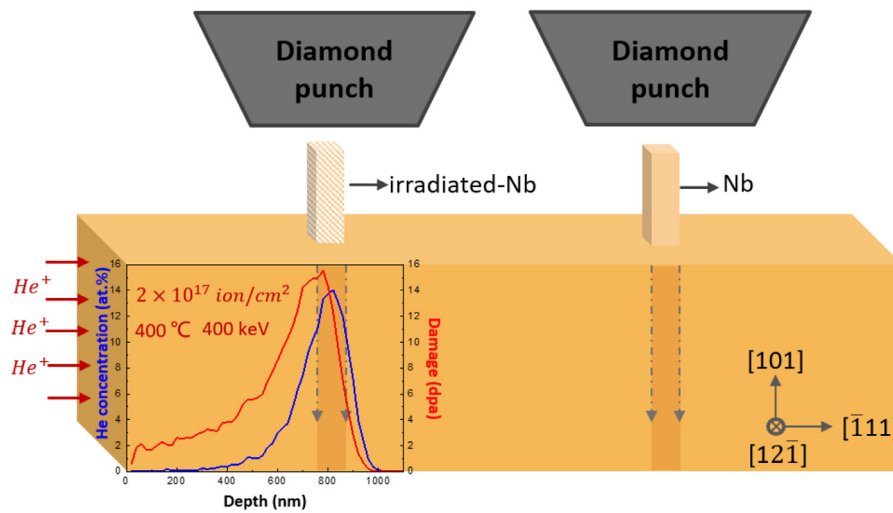


Fig. 1. Schematic of the helium ion implantation and micro-scale sample cutting processes used on the Nb single crystal. The variation in damage and helium concentration with the implantation depth calculated by the SRIM simulations are also plotted.

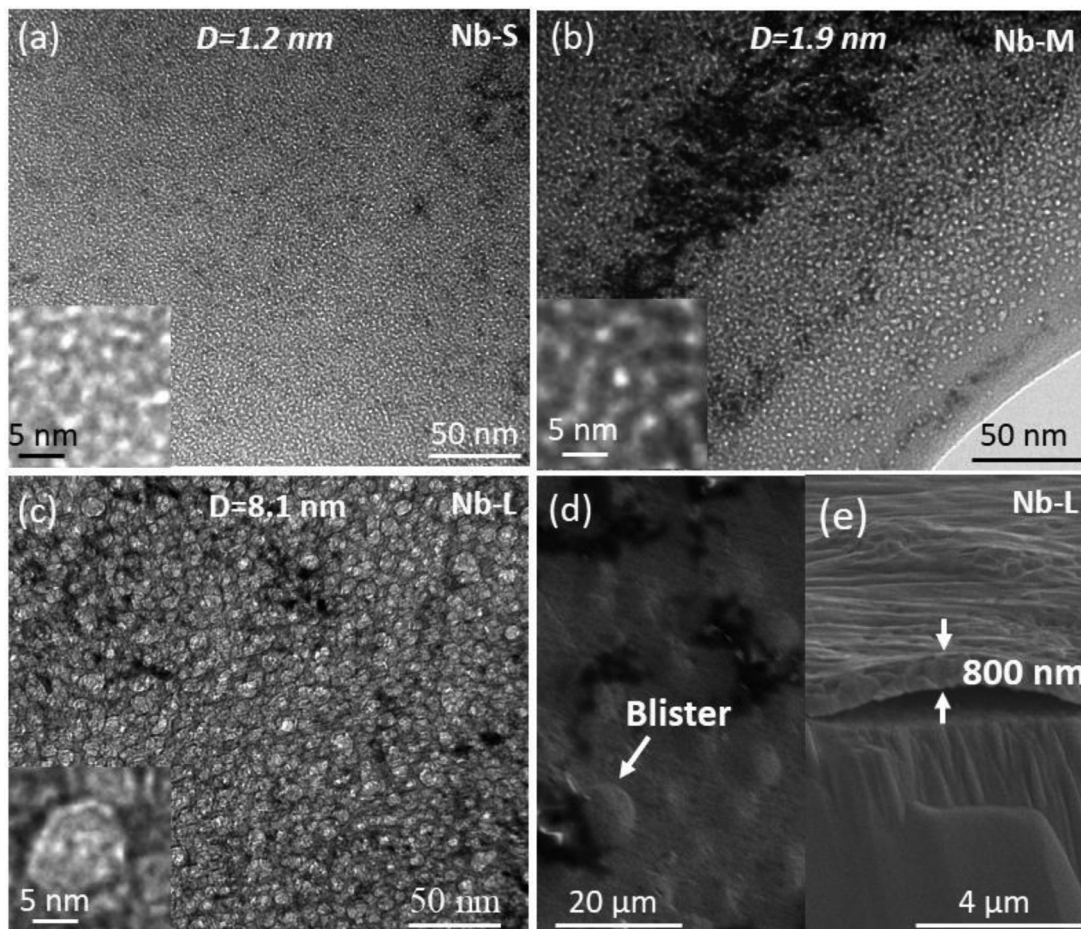


Fig. 2. Irradiation-induced helium bubbles and ion-implantation-induced surface blistering in Nb single crystal (a) Nb-S, (b) Nb-M, (c) Nb-L, and a (d) close up of surface blistering in Nb-L. The insets in the figures are highlight of the helium bubbles.

marked by arrows in Fig. 3(d). The Nb-S pillar, in contrast, exhibits homogeneous deformation, forming a smooth deformation front.

Fig. 3(f)–(h) show the pillars before and after tension. Under tension loading, the pure Nb pillar has a yield stress of 0.92 GPa, which is much smaller than the yield stress of 1.44 GPa in compression. As in compression, a series of strain bursts dominant the plastic flow in tension. The Nb-S pillar, on the other hand, displays

a very high yield stress of 3.07 GPa, and stable plastic flow, albeit for a short strain range, and finally fractures. Compared to the Nb-S pillar, the pure Nb pillar shows a much larger total elongation and necking. In the necked region, the sample has thinned down, and dislocations have accumulated. In contrast, the Nb-S pillar maintains its original width and the fracture surface is faceted along the (112) and (110) planes, which are known preferred slip planes

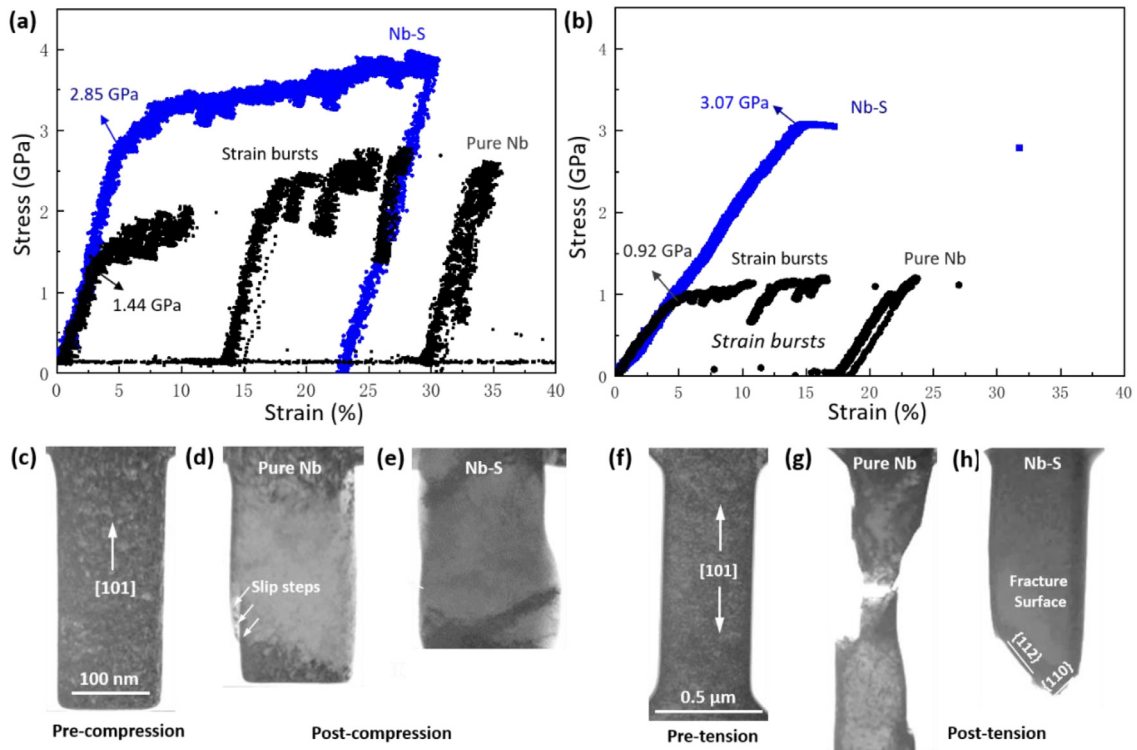


Fig. 3. Compressive and tensile behavior of the pure Nb and Nb-S pillars. (a) compressive stress-strain curves; (b) tensile stress-strain curves; (c) as-prepared rectangle pillar with a [110] orientation; (d) compressed pure Nb pillar; (e) compressed Nb-S pillar; (f) as-prepared tensile sample with a [110] orientation; (g) pulled pure Nb pillar; (h) pulled Nb-S pillar.

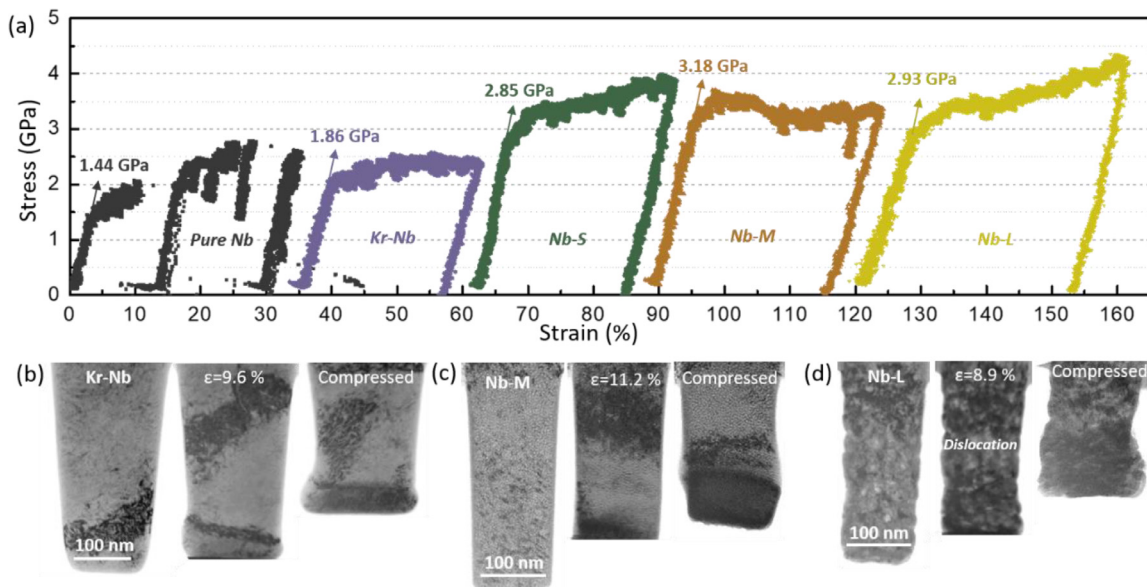


Fig. 4. Comparison of the pillars containing different sizes and concentrations of helium bubbles; (a) compressive strain-stress curves of Nb pillars with and without irradiation; (b) snapshots of the compressive of Kr irradiated pure Nb pillar; (c) snapshots of the compressive of Nb-M pillar; (d) snapshots of the compressive of Nb-L pillar.

in Nb [2]. Comparisons of pure Nb with Nb-S has clearly shown that irradiation hardening is significant in Nb, doubling the yield strength in compression and increasing it 3.3 times in tension.

3.3. Compressive behaviors of Nb pillar with different size He bubbles

Fig. 4(a) compares the compression engineering strain-stress curves of the pure Nb, Kr-Nb, Nb-S, Nb-M, Nb-L pillars. Table 1 summarizes the radiation conditions for these four types of sam-

ples. From their strain-stress curves, the yield stress can be determined as the stress at 0.2% flow stress. Accordingly, the yield strengths of the pure Nb, Kr-Nb, Nb-S, Nb-M, Nb-L pillars are 1.44 GPa, 1.86 GPa, 2.85 GPa, 3.18 GPa, 2.93 GPa, respectively. Accordingly, the amount of irradiation hardening associated with the Kr-Nb, Nb-S, Nb-M, Nb-L samples are 0.42 GPa, 1.41 GPa, 1.74 GPa, 1.49 GPa, respectively. The He irradiated pillars show a much larger hardening increment than the Kr-Nb pillar.

Table 1
Radiation conditions and yield stresses of the Nb pillars with different helium implantation histories.

Radiation condition/ a_{VS} Sample	Fluence Temperature (ion/cm^2) ($^{\circ}\text{C}$)	Ion energy (keV)	Heat treatment	Yield stress (GPa)
pure Nb	0 400	400	No	1.44
Nb-S	2×10^{17} 400	400	No	2.85
Nb-M	5×10^{17} 400	400	No	3.18
Nb-L	5×10^{17} 400	400	1000 for 1h	2.93

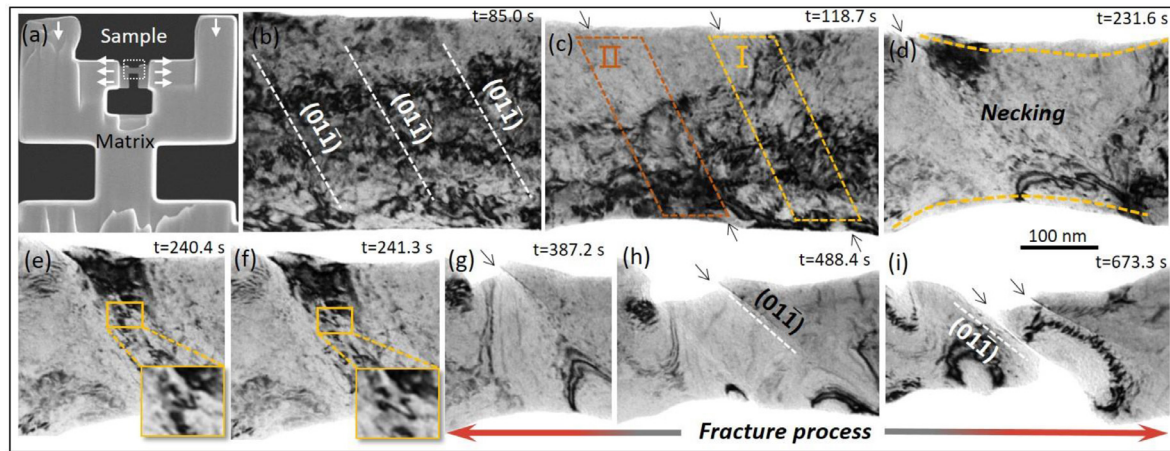


Fig. 5. Deformation mechanisms in the pure Nb pillar. (a) push-to-pull sample. (b) to (d) activation of slip in the $(01\bar{1})$ plane and formation of slip steps. Slip localization occurs in region I and II in (c). (e) and (f) evidence of dislocation emission. (g) to (i) slip-induced fracture in pure Nb pillar.

Toward understanding the differences, Fig. 4(b)–(d) present the stages of compression processes for the Kr-Nb, Nb-M, and Nb-L pillars. All these samples demonstrate continuous plasticity and stable deformation. Differences in hardening could be related to the distinct irradiation defects in these samples. In the Kr-Nb sample, which was irradiated to 23.4 dpa, the main irradiation defects are dislocation loops. In the He irradiated samples, operation of both the (110) and $(11\bar{2})$ slip planes were observed. The increment in the CRSS $\Delta\tau$ for these two $\{110\}\langle 111\rangle$ and $\{11\bar{2}\}\langle 111\rangle$ slip systems was estimated using three common models and they are compared with the experimentally measured $\Delta\tau$ in Table 3. The actual $\Delta\tau$ are at least 3 times larger than the model estimates. For Nb, the irradiation hardening in the He irradiated Nb pillar is remarkable and unexpected.

3.4. Dislocation dynamics in strained pure Nb, Nb-S, and Nb-L pillars

The dislocation activities in Nb pillars containing different sizes of He bubbles were investigated using *in-situ* nanomechanical techniques. To circumvent the vibrations that commonly occur when straining thin samples, we instead cut push-to-pull (PTP) samples to study the dislocation activities in irradiated Nb, as shown in Fig. 5(a). Pushing the two ends of the pillars generates a tensile strain in the middle of the tensile sample [32].

Figs. 5–7 display the microstructure evolution and deformation processes during the *in-situ* PTP tests of pure Nb, Nb-S and Nb-L pillars, respectively. In the uniform deformation stage for the pure Nb pillar, many dislocations glide along the $(10\bar{1})$ plane, as marked in Fig. 5(b). Thereafter, localized slip occurred in two regions at the onset of necking, as labeled in Fig. 5(c),(d). As can be seen in Movie S1, these dislocations initiate from the surface edges of the sample and slip unhindered across the entire pillar. The surface dark contrasts are defects produced during FIB cutting, which were cleaned away by dislocations during straining. With further straining, shear occurs along a localized slip band, as marked in Fig. 5(e),(f). The Movie S1 captures continuous operation of a dislocation source along this localized band, as highlighted in Fig. 5(e). Due to the

glide of numerous dislocations of the surface in the band, a sharp slip step is produced at the edge of sample, as shown in Fig. 5(g)–(i). With further loading, the shearing of pure Nb along several parallel (011) slip planes occurs, and finally the sample fractured along a (011) slip plane in the middle of the sample, as marked in Fig. 5(i).

For comparison, Fig. 6 shows the details of deformation in the Nb-S pillar. He bubbles in the Nb-S are very small and, as indicated by the white arrows in Fig. 6(a), can hardly be identified. They are preferentially distributed on the low index planes. Upon tensile loading, dislocation glide via multiple slip systems occurs, including the (110) , $(01\bar{1})$, and (211) , as marked in Fig. 6(b)–(d). In some cases, dislocation glide stops within the interior of the Nb-S pillar and cannot continue across the sample, as shown in Fig. 6(c)–(f). Also, unlike in pure Nb, some dislocations form within the interior of sample (Movie S2). He bubbles are known to serve as internal dislocation sources [17–19], and these interior dislocations most likely originated from the tiny He bubbles. With further loading, slip localizes along some of the slip planes, such as the (110) plane in Fig. 6(h). Some edge cracks can be seen here as well, although they do not have a special crystallographic character (Fig. 6(h)). Eventually, as marked in Fig. 6(j), the Nb-S pillar finally forms a zigzag fracture front along the low index planes. The faceted, crystallographic fracture surface is a likely consequence of the fact that He bubbles preferred to distribute along these low index planes and tended to coalescence and evolved into crack. As shown in Fig. 6(i), from the final stage, we observe that He bubble coarsening clearly took place during the tensile loading. Some He bubbles are 8 nm, which is six times the initial average size (1.2 nm). The increase in He bubble size could have resulted from coarsening and coalescence induced by dislocation-bubble interactions, which was seen previously in He irradiated Cu [17,18].

Comparing the deformation of the pure Nb and Nb-S pillars reveal many key differences resulting from He irradiation of Nb. We noticed that, first, at low strains, pure Nb pillar initiates a single slip system, while Nb-S pillar activates multiple slip systems. Second, dislocations nucleate from the edge of the pure Nb pil-

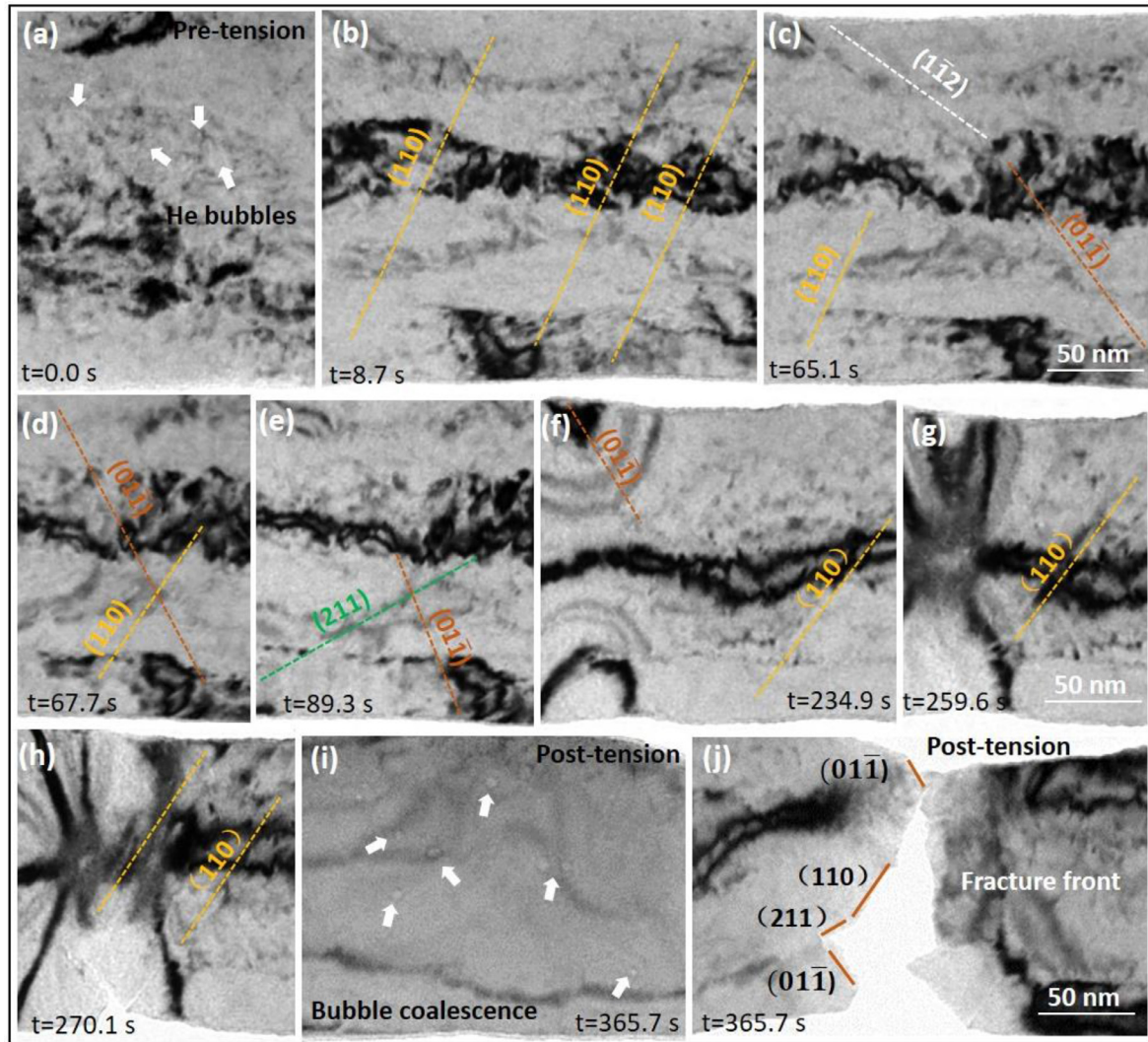


Fig. 6. Deformation mechanisms in the Nb-S sample. (a) helium bubbles in Nb-S; (b) to (h) activation of multiple slip systems upon loading; (i) deformation-induced helium bubble coarsening; (j) fracture of the Nb-S sample and its faceted fracture front.

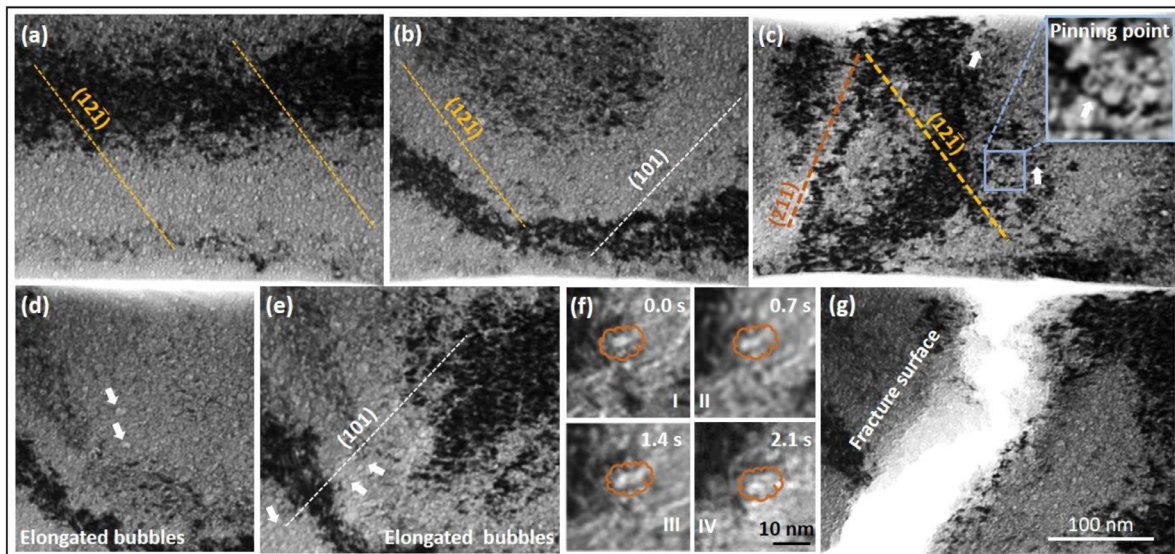


Fig. 7. Deformation mechanisms in the Nb-L sample. (a) to (c) dislocation-helium bubble interaction; (d) to (f) coalescence and fragmentation of the helium bubbles during tension; (g) irregular fracture front in the Nb-L sample.

lar, while in the Nb-S pillar, dislocation can also form within the sample, likely because the He bubbles served as dislocation sources [17,31]. Third, dislocation slip localizes within a few bands in pure Nb, whereas dislocation slip is distributed across the entire gauge section in the Nb-S pillar. Fourth, some slip lines terminate inside the Nb-S pillar instead of running through the entire sample like in the pure Nb pillar. Finally, the pure Nb pillar fractures along one crystallographic plane, while the Nb-S pillar have a faceted fracture surface. These differences in the deformation behavior of pure Nb and Nb-S pillar indicate that the He bubbles significantly alter the dislocation activities and failure mode in Nb.

By increasing the initial He bubbles size by four times to 8 nm in the Nb-L pillar, we find that the deformation mechanisms of the Nb pillars change remarkably, as shown in Fig. 7 for Nb-L pillar. Upon tensile loading, numerous dislocations emit from the He bubbles and accommodate plastic deformation [17,18]. None of these dislocations can slip across the pillar, and no slip line can be clearly identified, as marked in Fig. 7(a)–(c) and seen in Movie S3. With further loading, we capture He bubble elongation and fragmentation, as marked in Fig. 7(d),(f). Fig. 7(f) shows an enlarged view of bubble elongation and fragmentation. In Fig. 7(f) I and II, the He bubble gradually elongates, while in III and IV, the elongated bubble fractures into two bubbles. Analysis of the final fracture in Fig. 7(g) shows that the fracture mode is completely different from that seen in the pure Nb and Nb-S pillars. Coalescence of the larger He bubbles and necking of the material ligaments between the bubbles induce the final fracture, as manifested by the flaky structures produced in the fracture front (Fig. 7(g)).

4. Discussion

He irradiated Nb pillars show remarkable hardening, several times higher than that reported for irradiated Cu and Zr [17,20]. In the following, we discuss and rationalize the mechanism behind such ultrahigh hardening in irradiated Nb, based on predictions by traditional hardening models and by tracking and partitioning the implanted He atoms in TEM-visible He bubble from those in the Nb lattice.

4.1. Hardening induced by the TEM-visible He bubbles

The hardening and embrittlement caused by irradiation defects are closely related to the interaction between gliding dislocations and defect clusters [35,36]. Several strengthening models have been proposed to calculate the change in dislocation glide resistance $\Delta\tau$ induced by irradiation defects, such as the dispersed barrier model (DBH), Friedel-Kroupa-Hirsch model (FKH) [36–39], Osetsky and Bacon model [35,40,41] and Friedel model [43]. Here we discuss application of the Friedel model to estimate $\Delta\tau$ resulting from the He bubbles. The other models were also used to determine $\Delta\tau$ with the same He bubble characteristics, but we find that the Friedel model predicts the highest $\Delta\tau$ among them.

The characteristics of the He bubbles needed for the model are measured based on TEM analysis and these are summarized in Table 2. Assuming the shape of the He bubbles is spherical and using the measured average bubble radius r , the bubble volume can be calculated as: $V_{\text{bubble}} = 4\pi r^3/3$. Given V_{bubble} , the bubble volume fraction is given by: $f_v = N_{\text{bubble}}V_{\text{bubble}}$, where N_{bubble} is the He bubble number density. For a fixed N_{bubble} , as the bubble size increases, f_v also increases. Also given N_{bubble} , we determine the center-to-center bubble spacing via: $l = 1/\sqrt{2rN_{\text{bubble}}}$ [35,37].

According to Friedel model, the critical $\Delta\tau$ for a dislocation to bypass a He bubble in its glide plane is [43]:

$$\Delta\tau = \frac{Gb}{2\pi l_s} \ln\left(\frac{l_s}{r\sqrt{\cos\varphi_c}}\right) (\cos\varphi_c)^{\frac{3}{2}} \quad (1)$$

where $l_s = l - 2r$ is the bubble surface spacing, G is the shear modulus, and b is the value of the Burgers vector. The angle φ_c is half critical bow-out angle of the dislocation cutting an obstacle and is given by $\cos\varphi_c = \ln(\alpha\bar{D}/b)/\ln(l_s/b)$, where $1/\bar{D} = 1/D_b + 1/l_s$, $D_b = 2r$ is the diameter of He bubbles and \bar{D} is a harmonic mean of l_s and D_b [43].

Applying the model to the He-implanted samples gives for $\varphi_c = 71.9^\circ$ for Nb-S, 65.2° for Nb-M, and 40.9° for Nb-L and the corresponding $\Delta\tau$ is 0.18 GPa, 0.27 GPa, and 0.34 GPa. The variations of $\Delta\tau$ and l_s with bubble size are plotted in Fig. 8 and listed in Table 3. In Fig. 8, the solid red star represents the average bubble spacing l , while the hollow star represents the bubble surface spacing l_s . As the average D_b increases, the l_s gradually decreases. The upper part of Fig. 8 reveals a large gap between the model $\Delta\tau$ and experimental measured value, in which $\Delta\tau$ only accounts for less than one third of the experimentally observed irradiation hardening. Clearly, hardening due to the observed He bubbles alone cannot predict well the substantial irradiation hardening in BCC Nb. This observation is like the ultrahigh hardening in He irradiated W [31].

4.2. Partitioning of the implanted He in the TEM-visible bubbles and the Nb lattice

Besides the TEM-visible He bubble hardening, we consider the notion that undetectable, atomic-scale He-defect clusters can provide hardening. Because of a strong binding between He atoms with irradiation-induced vacancies (-1.75 eV) in Nb, the implanted He ions are deeply trapped in the sample once they form into clusters. Even annealed at 1000 °C for 1 h, the peak He concentration still locate at the depth of ~800 nm (See Fig. 2(d)). Owing to the formation of very stable He-V complexes, He leaking is hardly occurring during sample preparation and storage, which provides a basis for us to estimate the partitioning of He in bubbles and in the Nb lattice. To determine how much He would be lying undetected in the Nb lattice, we first estimate the amount of implanted He atoms in the TEM-visible He bubbles. An estimate for the pressure in a He bubble is given by: $P = 2\gamma/r + \sigma$, where γ is the surface energy and σ is the stress around the bubble [42]. For a lower bound estimate, we consider the pressure at equilibrium in which $\sigma = 0$, which gives $P_{\text{low}} = 2\gamma/r$. A practical upper bound is provided by the condition needed for dislocation punching, which is $\sigma = \mu b/r$, giving $P_{\text{high}} = 2\gamma + \mu b/r$ [43]. For pure Nb, where $\mu = 37.5$ GPa, $\gamma = 2.69$ Jm⁻², and $b = 2.68$ nm, the upper and lower pressure bounds for the He bubbles in the Nb-S, Nb-M, and Nb-L samples are 8.95–26.83 GPa, 5.65–16.94 GPa, and 1.33–3.97 GPa, respectively [43].

Given the pressure of He bubbles, one of two methods can be used to estimate the number of He atoms in one bubble. The first method is based on the empirical equation-of-state (EOS) for the high-pressure behavior of He obtained by Mill [44]:

$$V_{\text{molar}} = \left(22.575 + 0.0064655T - 7.2645T^{-\frac{1}{2}}\right)P^{-\frac{1}{3}} \\ + (-12.483 - 0.024549T)P^{\frac{2}{3}} \\ + \left(1.0596 + 0.10604T - 19.641T^{-\frac{1}{2}} + 189.84T^{-1}\right)P^{-1} \quad (2)$$

where V_{molar} is the molar volume and $T = 298$ K. The number of He atoms in a single He bubble is $N_{\text{He}} = N_A V_{\text{bubble}}/V_{\text{molar}}$, so that the number of He atoms per bubble for Nb-S, Nb-M, Nb-L samples are 161, 554, and 27136, respectively [35,42]. The ratio of He in the He bubbles to the total implanted He can be calculated according to $R_{\text{He}} = N_{\text{He}}N_{\text{bubble}}/N_{\text{sample}}$, where R_{He} is the ratio of He in the bubbles to all implanted He in the sample. The total number

Table 2
Characteristics of the helium bubbles in the Nb-S, Nb-M, Nb-L samples.

Bubble/Parameter	Nb-S	Nb-M	Nb-L
Average bubble diameter (nm)	1.2 ± 0.3	1.9 ± 0.2	8.1 ± 1.3
Average bubble density (*10 ²³ /m ³)	12.6	9.9	3.02
Volume of one typical He bubble (nm ³)	0.90	3.59	278.12
Bubble Volume fraction (%)	0.11	0.36	8.4
Bubble spacing, l _s (nm)	25.72	23.06	20.22
Helium atom number in each bubble	161 ¹³⁷ yi89 ³⁵¹	554 ¹³⁷ i/754 ³⁵¹	27136 ^{E37} /27534 ¹³⁵
Vacancy number in each bubble	50.33	199.76	15477.42
Ratio of He atoms to vacancies	3.20 ¹³⁷ /3.76 ¹³⁵¹	2.77 ¹³⁷ /3.77 ³⁵¹	1.75 ³⁷ /1.78 ¹³⁵¹
Percentage of He in bubble (%)	4.55 ¹³⁷ /5.34 ¹³⁵¹	3.32 ¹³⁷ /4.51 ³⁵¹	49.55 ³⁷ /50.27 ³⁵¹
Bubble pressure (GPa)	8.95	5.65	1.33

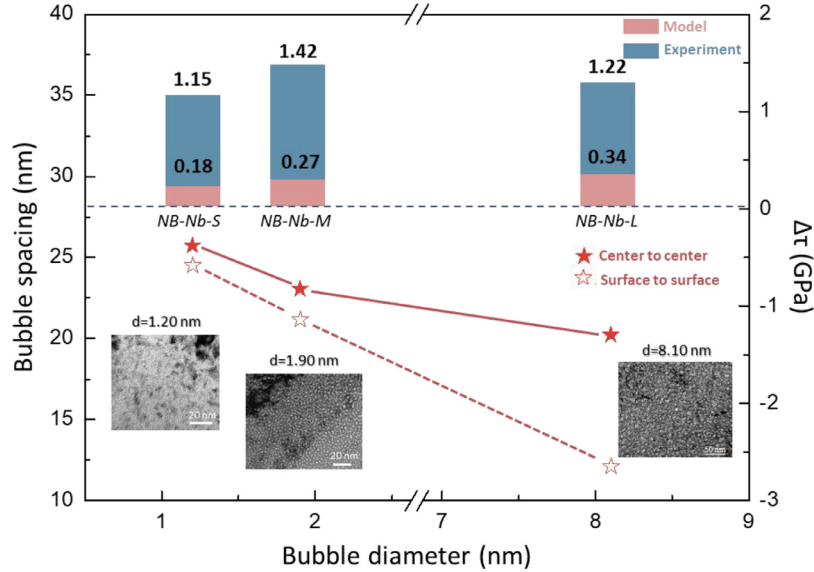


Fig. 8. Irradiation hardening in the Nb pillars with different sizes and spacings of helium bubbles. Model calculations for helium bubble strengthening is inserted for comparison. The inset TEM images show helium bubbles in the three types of samples.

Table 3
Comparison of the measured critical resolved shear stresses enhancement with different model predictions.

Experiment model/Sample	Bacon- Orowan model $\Delta\tau$ (GPa)	Friedel equation $\Delta\tau$ (GPa)	DBH model $\Delta\tau$ (GPa)	Experimental enhancement {110} $\Delta\tau$ (GPa)	Experimental enhancement {112} $\Delta\tau$ (GPa)
Nb-S	0.06	0.18	0.21	1.15	1.00
Nb-M	0.07	0.27	0.23	1.42	1.24
Nb-L	0.26	0.34	0.26	1.22	1.06

of implanted He is $N_{sample} = D_{He}FV$, where D_{He} is the implanted He ions (atoms·cm⁻³)/(atoms·cm⁻²) that can be obtained from the SRIM simulation in Fig. 1, F is the irradiation fluence (atoms·cm⁻²), and V is the sample volume. Using the upper bound pressure estimate, the corresponding upper bound on R_{He} is 4.549% for Nb-S, 3.316% for Nb-M, and 49.55% for Nb-L. These estimates suggest that a vast majority of the He lies outside the bubbles [31].

The second method begins by estimating the He density ρ based on the bubble pressure, and then multiplying by the He bubble volume [45,46]. An approximate He density is $\rho = 209$ atom·nm⁻³ for the Nb-S sample, $\rho = 210$ atom·nm⁻³ for the Nb-M sample, and $\rho = 99$ atom·nm⁻³ for the Nb-L sample. Using the relation, $N_{He} = V_{bubble}\rho$, we obtain the number of He atoms per He bubble, which are 189 for Nb-S, 754 for Nb-M, and 27.5×10^3 for Nb-L [45,46]. The corresponding ratios of He atoms R_{He} are 5.34% for Nb-S, 4.51% for Nb-M, 50.27% for Nb-L. The second method tends to overestimate the He density [43], and thus these ratios are expected to be larger than that obtained by the first

method. Nevertheless, these calculations again reveal that most of the implanted He atoms are still stored inside the Nb lattice.

Furthermore, for the number of vacancies in each bubble can be estimated by $N_{vacancy} = V_{bubble}N_{Nb}$, where N_{Nb} is the atomic density of Nb, 55.65/nm³, giving 50.33 for bubbles in Nb-S, 199.76 for those in Nb-M, $15,477 \times 10^3$ for those in Nb-L. Finally, taken together, we can determine the ratio of He atoms to vacancies per bubble, which is 3.20 for bubbles in Nb-S, 2.77 for those in Nb-M, and 1.75 for those in Nb-L, as plotted in Fig. 9(a). Thus, the bubbles are mostly He. Despite this, the He in these bubbles are only a fraction of the He that has been implanted in the sample.

4.3. Hardening induced by the undetected point-defect complexes

The mismatch between experimental measurement and conventional model analysis suggests that sources of hardening apart from the bubbles detected by TEM exist. It has been proposed that because the binding energy of He atom and vacancy is high, i.e.,

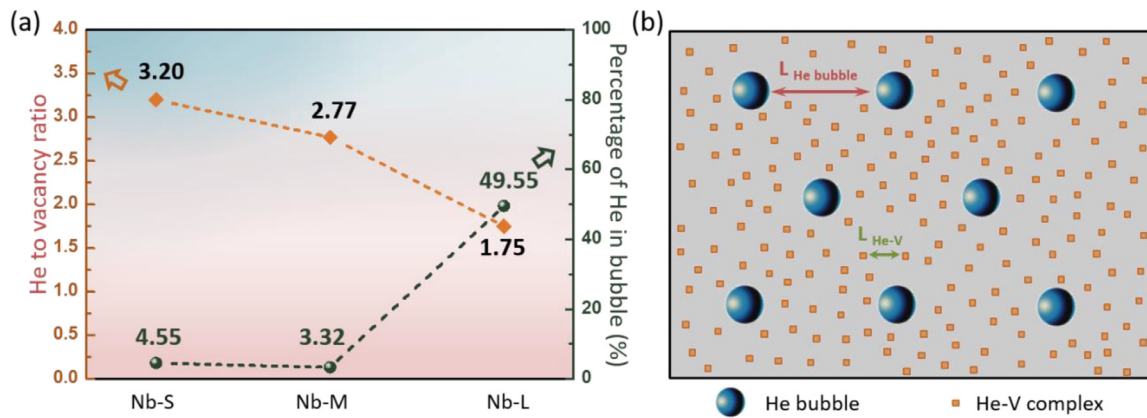


Fig. 9. (a) Helium-to-vacancy ratio and percentage of helium atoms in the bubbles; (b) illustration of irradiation defects in Nb with both TEM-visible helium bubbles and high densities of TEM-invisible He-V complexes. High densities of He-V complexes obstruct the glide of dislocations, which is proposed here as the origin of the anomalous hardening in helium-irradiated Nb.

–1.75 eV [47–55], a large amount of stable He-V complexes can form during He implantation [56–64]. We suspect that most of these complexes lie sessile in the lattice and are too small to be resolved under high resolution-TEM observation. It was reported that the dynamic formation of oxygen-vacancy complexes triggers significant hardening in Nb [2]. The hardening observed here is of a similar nature. Therefore, the large amount of stable He-V complexes is the likely source of additional hardening, particularly if the binding energy between dislocations and point defect complexes is strong [31].

The interaction between He-V complexes and dislocations have been estimated by simulation methods [60–63]. The interaction of He-V clusters and edge dislocations depends on the He/V ratio, the position of the clusters relative to the slip plane, the cluster size, and temperature [60]. Simulations show that He-V clusters in α -Fe are very stable and do not move along with the dislocation, even at 600 K [60]. In addition, also in α -Fe, the ratio of n to m in the He_nV_m clusters can influence the interaction between He-V complexes and $a/2\langle 111 \rangle\{110\}$ edge dislocations [61]. When the ratio is greater than 1, the clusters become trapped in the dislocation core on the tension side. However, once the ratio is less than 1, the clusters are trapped within ~ 0.5 nm from the dislocation core on both the compression and tension sides [61]. The binding energies of the He_nV_m clusters to the dislocation depends on the He/V ratio, as well, for $n/m > 1$. However, when $n/m < 1$, the binding energies of the He_nV_m clusters to the dislocation depends not only on the He/V ratio, but also on the cluster size [61]. In α -Fe both interstitial He atoms and single vacancies can be attracted to and trapped at the $\langle 111 \rangle$ screw dislocations [63]. Because both vacancies and He atoms can be trapped in screw dislocations but otherwise have high mobility, screw dislocations are sinks for He bubbles and He-V complexes. At the same time, the lower mobility of the complexes within the screw dislocations can, in turn, strongly trap these dislocations [63].

Moreover, the ultrahigh hardening in He irradiated Nb is also related to the dynamic formation of He-V complexes. For BCC pure metals, many vacancy and interstitial atoms can be produced during screw dislocation glide [65,66]. Under an applied shear stress of 1.5 GPa, the screw dislocation moves via double kinks or cross kink nucleation and propagation, which leads to the interaction among kinks formed on different glide planes, and thus promotes the formation of Frenkel pairs in Fe [67–69]. Other simulations and experiments also show that the vacancies are generated during screw dislocation movement in BCC metals under high stresses or high strain rates [70–72]. In addition, because of the chemical effect of He interstitials, the formation energy of vacancies in

Nb can be lowered by 50% in pure Nb [47]. Therefore, any excess He atoms can easily cluster to the large number of vacancies either irradiation-induced or triggered by screw dislocation glide and these He-V clusters can tend to lock mobile dislocations or resist their glide, which would partially contribute to the observed irradiation hardening in Fig. 8. It may be that the *in-situ* compressive tests of samples with low and medium He concentration show noticeably much higher strengthening than the Kr-Nb sample due to the lack of He-V complexes in the latter sample. When faced with many atomic-scale He-V complexes distributed throughout the material, particularly if more finely spaced than the He bubbles, dislocations need much higher stress to bow out in between and overcome them, as illustrated in Fig. 9(b).

To estimate the strengthening contribution of such complexes, we take Nb-S sample as an example. Due to the strong trapping effect of He-V complexes on dislocation, we can calculate the average spacing of He-V complexes according to the hardening obtained by experiments. The average spacing between He-V complexes can be estimated based on Orowan's equation [31,73–75]:

$$l_{\text{He-V}} = \frac{\alpha G b}{2\pi\sqrt{1-\nu}\Delta\tau} \ln\left(\frac{r_0}{b}\right) \quad (3)$$

where α is a constant in the range of 0.1–0.5 for weak obstacles [74], ν is Poisson's ratio of Nb, $\Delta\tau = 0.97$ GPa is the hardening induced by the proposed He-V complexes, $r_0 = 2$ nm is the outer radius of dislocation core (comparable to He bubble size), and as before, G is shear modulus, b is the Burgers vector value. Therefore, the average spacing between He-V complexes in Nb-S sample is 1.06 nm. The radius of He-V complexes can be further estimated by calculating the number of He atoms of each cluster in the samples, when given that the volume of the sample is $V = 6.69 \times 10^6$ nm³. Accordingly, the number of He atoms in the He-V complexes in the sample can be calculated from the following:

$$N_{\text{He-complex}} = (D_{\text{He}}F - N_{\text{bubble}}N_{\text{He}}) \times V \quad (4)$$

where $D_{\text{He}} = 4.108 \times 10^4$ (atom·cm⁻³)/(atom·cm⁻²) is the average implanted He ions at a given depth. The radiation fluence is $F = 2 \times 10^{17}$ atom·cm⁻², the number of bubbles per unit volume $N_{\text{bubble}} = 1.26 \times 10^{18}$ cm⁻³, and the number of He atoms per bubble is $N_{\text{He}} = 161$ atom. The calculation reveals that the number of He atoms remaining in Nb lattice is 5.36×10^7 . If, for example, the spacing between He-V complexes is 1.06 nm, then the number of He atoms in each cluster is approximately 1.5. Further, if each complex consist of one vacancy and one He, then the size of each complex is about 0.3 nm. Such He-V complexes with a size of 0.3 nm would be invisible under high-resolution-TEM observation. The He-

V complexes, therefore, must be distributed throughout the Nb lattice, each with a cluster size that lies below the resolution of TEM. The spacing between He-V complexes is only slightly larger than 1 nm, which as demonstrated earlier in Eq. (3), is small enough to induce the exceptionally high hardening, i.e., $\Delta\tau = 0.97$ GPa, seen in Fig. 8. Because each vacancy can store up to nine, He atoms in Nb in a complex [57], even when we increase the He concentration to 2 to 3 times that of the Nb-S sample, there would still be sufficient space to account for all the implanted He atoms. Because of the strong binding between He and vacancy [47–55], their mobility would be very low, and thus they could still be immobile in the Nb lattice, even after annealing at 1000 °C.

5. Conclusions

In this work, we investigated the mechanisms underlying He irradiation hardening in Nb based on a series of *in-situ* uniaxial tensile and compressive tests, defect evolution through *in-situ* push to pull tests and theoretical analysis. The main findings are:

1. He irradiation induces a more than two-fold increase in yield stress.
2. Compared with pure Nb, the He irradiated Nb pillars exhibit a different deformation mode. During the compression process, He bubbles enhance the deformation stability (less strain bursts) of the sample. In tension, He bubbles accelerate the fracture process.
3. Single crystal pure Nb pillars deform via activation of a single slip $\{110\}\langle 111 \rangle$ system originating from the surface, while He irradiated Nb initiates multiple slip $\{110\}\langle 111 \rangle$ and $\{112\}\langle 111 \rangle$ systems originating in the interior of the sample. He bubbles promote dislocation nucleation on these non-planar slip modes.
4. The size of He bubbles have a significant effect on the failure mode. The Nb-S pillars, with small 1–2 nm size bubbles, fail by bubble coalescence and form a faceted fracture surface, which is related to the distribution of He bubbles along special low-index crystallographic planes. In contrast, the Nb-L pillars, with 8 nm size bubbles, fail by bubble elongation and fragmentation, and the fracture surface contains flaky structures.
5. A large gap between model prediction for strengthening by TEM-detected He bubbles, and experimental measurement reveals a missing hardening component. Because of a strong binding of He atoms with vacancies, we propose that the implanted He ions are deeply trapped in the Nb lattice in the form of He-V complexes, which are likely the origins of the ultrahigh irradiation hardening in He irradiated Nb.

Declaration of Competing Interest

The authors declare no competing financial interests.

Acknowledgments

This research was supported by the National Natural Science Foundation of China (Grant Nos. 51922082, 51971170 and 51942104), the National Key Research and Development Program of China (2017YFB0702301), the 111 Project of China (Grant No. BP2018008) and the Innovation Project of Shaanxi Province (Grant No. 2017KTPT-12).

Supplementary materials

Supplementary material associated with this article can be found, in the online version, at doi:10.1016/j.jad.2018.04xs.077.

References

- [1] S.J. Zinkle, G.S. Was, Materials challenges in nuclear energy, *Acta Mater.* 61 (2013) 735–758.
- [2] P.J. Yang, Q.J. Li, T. Tsuru, S. Ogata, J.W. Zhang, H.W. Sheng, Z.W. Shan, G. Sha, W.Z. Han, J. Li, E. Ma, Mechanism of hardening and damage initiation in oxygen embrittlement of body-centred-cubic niobium, *Acta Mater.* 168 (2019) 331–342.
- [3] S. Mahajan, B.L. Eyre, Formation of dislocation channels in neutron irradiated molybdenum, *Acta Mater.* 122 (2017) 259–265.
- [4] O.E. Atwani, E. Esquivel, M. Efe, E. Aydogan, Y.Q. Wang, E. Martinez, S.A. Maloy, Loop and void damage during heavy ion irradiation on nanocrystalline and coarse grained tungsten: microstructure, effect of dpa rate, temperature, and grain size, *Acta Mater.* 149 (2018) 206–219.
- [5] X.O. Yi, M.L. Jenkins, M.A. Kirk, Z.F. Zhou, S.G. Roberts, *In-situ* TEM studies of 150 keV W⁺ ion irradiated W and W-alloys: damage production and microstructural evolution, *Acta Mater.* 112 (2016) 105–120.
- [6] Y. Chen, K.Y. Yu, Y. Liu, S. Shao, H. Wang, M.A. Kirk, J. Wang, X. Zhang, Damage-tolerant nanotwinned metals with nanovoids under radiation environments, *Nat. Commun.* 6 (2015) 7036.
- [7] D. Kiener, P. Hosemann, S.A. Maloy, A.M. Minor, *In situ* nanocompression testing of irradiated copper, *Nat. Mater.* 10 (2011) 608–613.
- [8] Y. Dai, M. Victoria, Defect cluster structure and tensile properties of copper single crystals irradiated with 600 MeV protons, *Mat. Res. Soc. Symp. Proc.* 439 (1997) 319–324.
- [9] Q.M. Wei, N. Li, K. Sun, L.M. Wang, The shape of bubbles in He-implanted Cu and Au, *Scr. Mater.* 63 (2010) 430–433.
- [10] M. Wang, I.J. Beyerlein, J. Zhang, W.Z. Han, Defect-interface interactions in irradiated Cu/Ag nanocomposites, *Acta Mater.* 160 (2018) 211–223.
- [11] S.J. Zinkle, J.T. Busby, Structural materials for fission & fusion energy, *Mater. Today* 12 (2009) 12–19.
- [12] E. Wakia, S. Jitsukawa, H. Tomita, K. Furuya, M. Sato, K. Oka, T. Tanaka, F. Takada, T. Yamamoto, Y. Kato, Y. Tayama, K. Shiba, S. Ohnuki, Radiation hardening and embrittlement due to He production in F82H steel irradiated at 250 °C in JMTR, *J. Nucl. Mater.* 343 (2005) 285–296.
- [13] G.R. Odette, M.Y. He, E.G. Donahue, P. Spatig, T. Yamamoto, Modeling the multiscale mechanics of flow localization–ductility loss in irradiation damaged bcc alloys, *J. Nucl. Mater.* 307–311 (2002) 171–178.
- [14] S.J. Zinkle, Fusion materials science: overview of challenges and recent progress, *Phys. Plasmas* 12 (2005) 058101.
- [15] F.A. Garner, M.B. Toloczko, B.H. Sencer, Comparison of swelling and irradiation creep behavior of fcc-austenitic and bcc-ferritic/martensitic alloys at high neutron exposure, *J. Nucl. Mater.* 276 (2000) 123–142.
- [16] H. Schroeder, H. Ullmaier, Helium and hydrogen effects on the embrittlement of iron- and nickel-based alloys, *J. Nucl. Mater.* 179–181 (1991) 118–124.
- [17] M.S. Ding, J.P. Du, L. Wan, S. Ogata, L. Tian, E. Ma, W.Z. Han, J. Li, Z.W. Shan, Radiation-induced helium nanobubbles enhance ductility in submicron-sized single-crystalline copper, *Nano Lett.* 16 (2016) 4118–4123.
- [18] W.Z. Han, M.S. Ding, Z.W. Shan, Cracking behavior of helium-irradiated small-volume copper, *Scr. Mater.* 147 (2018) 1–5.
- [19] M. Rafique, S. Chae, Y.S. Kim, Microstructural features and mechanical properties of 18 MeV He⁺ ions irradiated pure Zr, *Mod. Phys. Lett. B* 30 (2016) 1650395.
- [20] S.M. Liu, S.H. Li, W.Z. Han, Effect of ordered helium bubbles on deformation fracture behavior of α -Zr, *J. Mater. Sci. Technol.* 35 (2019) 1466–1472.
- [21] S.H. Li, J. Zhang, W.Z. Han, Helium bubbles enhance strength and ductility in small-volume Al-4Cu alloys, *Scr. Mater.* 165 (2019) 112–116.
- [22] H. Kayano, S. Yajima, Neutron irradiation effects on mechanical properties of niobium, *J. Nucl. Sci. Technol.* 12 (2012) 253–255.
- [23] M.J. Makin, F.J. Minter, The mechanical properties of irradiated niobium, *Acta Metall.* 7 (1959) 361–366.
- [24] M.S. Wechsler, R.P. Tucker, R. Bode, Radiation hardening in single crystal niobium—the temperature dependence of yielding, *Acta Metall.* 17 (1969) 541–551.
- [25] W.Q. Chen, X.Y. Wang, X.Z. Xiao, S.L. Qu, Y.Z. Jia, W. Cui, X.Z. Cao, B. Xu, W. Liu, Characterization of dose dependent mechanical properties in helium implanted tungsten, *J. Nucl. Mater.* 509 (2018) 260–266.
- [26] H. Tanigawa, R.L. Klueh, N. Hashimoto, M.A. Sokolov, Hardening mechanisms of reduced activation ferritic/martensitic steels irradiated at 300 °C, *J. Nucl. Mater.* 386–388 (2009) 231–235.
- [27] Y.N. Osetsky, R.E. Stoller, Atomic-scale mechanisms of helium bubble hardening in iron, *J. Nucl. Mater.* 465 (2015) 448–454.
- [28] L.X. Jia, X.F. He, S. Wu, D.J. Wang, H. Cao, Y.K. Dou, W. Yang, Study of helium bubble induced hardening in BCC-Fe by molecular dynamics simulation, *Mater. Sci. Forum* 944 (2019) 378–386.
- [29] J.A. Donovan, R.J. Burger, R.J. Arsenal, The effect of helium on the strength and microstructure of niobium, *Metall. Trans. A* 12 (1981) 1917–1922.
- [30] A.V. Veen, H. Eleveld, M. Clement, Helium impurity interactions in vanadium and niobium, *J. Nucl. Mater.* 212–215 (1994) 287–292.
- [31] R.Y. Zheng, R.W. Jian, I.J. Beyerlein, W.Z. Han, Atomic-scale hidden point-defect complexes induce ultrahigh-irradiation hardening in tungsten, *Nano Lett.* (2021).
- [32] M.S. Ding, L. Tian, W.Z. Han, J. Li, E. Ma, Z.W. Shan, Nanobubble fragmentation and bubble-free-channel shear localization in helium-irradiated submicron-sized copper, *Phys. Rev. Lett.* 117 (2016) 215501.

- [33] D.Y. Lin, H.F. Song, X.D. Hui, Molecular dynamics simulation of threshold displacement energy and primary damage state in niobium, *Condens. Matter* 1702 (2017) 03598.
- [34] R.Y. Zheng, W.Z. Han, Comparative study of radiation defects in ion irradiated bulk and thin-foil tungsten, *Acta Mater.* 162–171 (2020) 186.
- [35] N. Li, M. Nastasi, A. Misra, Defect structures and hardening mechanisms in high dose helium ion implanted Cu and Cu/Nb multilayer thin films, *Int. J. Plast.* 32–33 (2012) 1–16.
- [36] S.J. Zinkle, Y. Matsukawa, Observation and analysis of defect cluster production and interactions with dislocations, *J. Nucl. Mater.* 329–333 (2004) 88–96.
- [37] L.K. Mansur, M.L. Grossbeck, Mechanical property changes induced in structural alloys by neutron irradiations with different helium to displacement ratios, *J. Nucl. Mater.* 155–157 (1988) 130–147.
- [38] B.N. Singh, A.J.E. Foreman, H. Trinkaus, Radiation hardening revisited: role of intracascade clustering, *J. Nucl. Mater.* 249 (1997) 103–115.
- [39] N. Li, E.G. Fu, H. Wang, J.J. Carter, L. Shao, S.A. Maloy, A. Misra, X. Zhang, He ion irradiation damage in Fe/W nanolayer films, *J. Nucl. Mater.* 389 (2009) 233–238.
- [40] U.F. Kocks, The theory of an obstacle-controlled yield strength-report after an international workshop, *Mater. Sci. Eng.* 27 (1977) 291–298.
- [41] Y.N. Osetsky, D.J. Bacon, Atomic-scale mechanisms of void hardening in bcc and fcc metals, *Philos. Mag.* 90 (2010) 945–961.
- [42] P. Landau, Q. Guo, P. Hosemann, Y.Q. Wang, J.R. Greer, Deformation of as-fabricated and helium implanted 100 nm-diameter iron nano-pillars, *Mater. Sci. Eng. A* 612 (2014) 316–325.
- [43] Q.M. Wei, N. Li, N. Mara, M. Nastasi, A. Misra, Suppression of irradiation hardening in nanoscale V/Ag multilayers, *Acta Mater* 59 (2011) 6331–6340.
- [44] R.L. Mills, D.H. Liebenberg, J.C. Bronson, Equation of state and melting properties of ^4He from measurements to 20 kbar, *Phys. Rev. B* 21 (1980) 5137–5148.
- [45] A. Polian, M. Grimsditch, Elastic properties and density of helium up to 20 GPa, *Europhys. Lett.* 2 (1986) 849–855.
- [46] C. Cazorla, J. Boronat, First-principles modeling of three-body interactions in highly compressed solid helium, *Phys. Rev. B* 92 (2015) 224113.
- [47] P.B. Zhang, T.T. Zou, J.J. Zhao, He-He and He-metal interactions in transition metals from first-principles, *J. Nucl. Mater.* 467 (2015) 465–471.
- [48] A. Bakaev, D. Terentyev, P. Grigorev, M. Posselt, E.E. Zhurkin, Ab initio study of interaction of helium with edge and screw dislocations in tungsten, *Nucl. Instrum. Methods Phys. Res. Sect. B* 393 (2017) 150–154.
- [49] P.B. Zhang, J.J. Zhao, Energetics and configurations of He-He pair in vacancy of transition metals, *Nucl. Instrum. Methods Phys. Res. Sect. B* 322 (2014) 34–40.
- [50] W.F.W.M. Heugten, L.M. Gaspers, J.T.M. Hosson, Atomic configuration of a $1/2\langle 111 \rangle$ -screw dislocation in pure Mo and in Mo containing He interstitials, *Phys. Status Solidi* 92 (1979) 199–209.
- [51] H.L. Heinisch, F. Gao, R.J. Kurtz, Atomistic modeling of helium interacting with screw dislocations in $\alpha\text{-Fe}$, *J. Nucl. Mater.* 367–370 (2007) 311–315.
- [52] H.L. Heinisch, F. Gao, R.J. Kurtz, E.A. Le, Interaction of helium atoms with edge dislocations in $\alpha\text{-Fe}$, *J. Nucl. Mater.* 351 (2006) 141–148.
- [53] P.B. Zhang, C. Zhang, R.H. Li, J.J. Zhao, He-induced vacancy formation in bcc Fe solid from first-principles simulation, *J. Nucl. Mater.* 444 (2014) 147–152.
- [54] W.F.W.M. Heugten, F.D. Berg, L.M. Gaspers, A. Veen, J.T.M. Hosson, The influence of interatomic potentials on the interaction of He with a $1/2\langle 111 \rangle\{110\}$ edge dislocation in molybdenum, *Phys. Status Solidi* 90 (1978) 643.
- [55] Y. Zhao, G. Lu, QM/MM study of dislocation-hydrogen/helium interactions in $\alpha\text{-Fe}$, *Model. Simul. Mater. Sci. Eng.* 19 (2011) 1–13.
- [56] M.A. Cerdeira, S.L. Palacios, C. Gonzalez, D. Fernandez-Pello, R. Iglesias, Ab initio simulations of the structure, energetics and mobility of radiation-induced point defects in bcc Nb, *J. Nucl. Mater.* 478 (2016) 185–196.
- [57] C. Gonzalez, M.A. Cerdeira, S.L. Palacios, R. Iglesias, Reduction of the repulsive interaction as origin of helium trapping inside a monovacancy in BCC metals, *J. Mater. Sci.* 50 (2015) 3727–3739.
- [58] L.J. Gui, Y.L. Liu, W.T. Wang, Y.N. Liu, K. Arshada, Y. Zhang, G.H. Lu, J. Yao, Behaviors of helium in vanadium: stability, diffusion, vacancy trapping and ideal tensile strength, *Prog. Nat. Sci. Mater.* 23 (2013) 459–463.
- [59] L. Yang, X.T. Zu, H.Y. Xiao, Y.S. Zheng, K.Z. Liu, F. Gao, Defect production and formation of helium-vacancy clusters due to cascades in $\alpha\text{-iron}$ [J], *Phys. B* 391 (2007) 179–185.
- [60] L. Yang, Z.Q. Zhu, S.M. Peng, X.G. Long, X.S. Zhou, X.T. Zu, H.L. Heinisch, R.J. Kurtz, F. Gao, Effects of temperature on the interactions of helium-vacancy clusters with gliding edge dislocations in $\alpha\text{-Fe}$, *J. Nucl. Mater.* 441 (2013) 6–14.
- [61] L. Yang, X.T. Zu, Z.G. Wang, F. Gao, X.Y. Wang, H.L. Heinisch, R.J. Kurtz, Interaction of helium-vacancy clusters with edge dislocations in $\alpha\text{-Fe}$, *Nucl. Instrum. Methods Phys. Res. Sect. B* 265 (2007) 541–546.
- [62] H.X. Xie, K. Xu, G.H. Lu, T. Yu, F.X. Yin, Trapping of hydrogen and helium at an $\{110\}\langle 111 \rangle$ edge dislocation in tungsten, *J. Nucl. Mater.* 484 (2017) 270–275.
- [63] H.L. Heinisch, F. Gao, R.J. Kurtz, Atomic-scale modeling of interactions of helium, vacancies and helium-vacancy clusters with screw dislocations in alpha-iron, *Philos. Mag.* 90 (2010) 885–895.
- [64] N. Gao, M. Victoria, J. Chen, H.V. Swygenhoven, Helium-vacancy cluster in a single bcc iron crystal lattice, *J. Phys. Condens. Matter* 23 (2011) 245403.
- [65] H. Mecking, Y. Estrin, The effect of vacancy generation on plastic deformation, *Scr. Metall.* 14 (1980) 815–819.
- [66] G. Henkelman, B.P. Uberuaga, H. Jonsson, A climbing image nudged elastic band method for finding saddle points and minimum energy paths, *J. Chem. Phys.* 113 (2000) 9901–9904.
- [67] H.J. Lee, B.D. Wirth, Molecular dynamics simulation of dislocation-void interactions in BCC Mo, *J. Nucl. Mater.* 386–388 (2009) 115–118.
- [68] J. Marian, W. Cai, V.V. Bulatov, Dynamic transitions from smooth to rough to twinning in dislocation motion, *Nat. Mater.* 3 (2004) 158–163.
- [69] J. Chaussidon, M. Fivel, D. Rodney, The glide of screw dislocations in bcc Fe: Atomistic static and dynamic simulations, *Acta Mater.* 54 (2006) 3407–3416.
- [70] Dutta A. Compressive deformation of Fe nanopillar at high strain rate: Modalities of dislocation dynamics, *Acta Mater.* 125 (2017) 219–230.
- [71] A. Stukowski, D. Cereceda, T.D. Swinburne, J. Marian, Thermally-activated non-schmid glide of screw dislocations in W using atomistically-informed kinetic monte carlo simulations, *Int. J. Plast.* 65 (2015) 108–130.
- [72] H.J. Lee, B.D. Wirth, Molecular dynamics simulation of dislocation-void interactions in BCC Mo, *J. Nucl. Mater.* 386–388 (2009) 115–118.
- [73] D.J. Bacon, U.F. Kocks, R.O. Scattergood, The effect of dislocation self-interaction on the Orowan stress, *Philos. Mag.* 28 (1973) 1241–1263.
- [74] G.E. Lucas, The evolution of mechanical property change in irradiated austenitic stainless steels, *J. Nucl. Mater.* 206 (1993) 287–305.
- [75] J. Zhang, W.Z. Han, Oxygen solutes induced anomalous hardening, toughening and embrittlement in body-centered cubic vanadium, *Acta Mater.* 196 (2020) 122–132.